A Data-driven Method for Transient Stability Margin Prediction Based on Security Region

Jun An, Jiachen Yu, Zonghan Li, Yibo Zhou, and Gang Mu

***Abstract*—Transient stability assessment (TSA) based on security region is of great significance to the security of power systems. In this paper, we propose a novel methodology for the assessment of online transient stability margin. Combined with a geographic information system (GIS) and transformation rules, the topology information and pre-fault power flow characteristics can be extracted by 2D computer-vision-based power flow images (CVPFIs). Then, a convolutional neural network (CNN)-based comprehensive network is constructed to map the relationship between the steady-state power flow and the generator stability indices under the anticipated contingency set. The network consists of two components: the classification network classifies the input samples into the credibly stable/unstable and uncertain categories, and the prediction network is utilized to further predict the generator stability indices of the categorized samples, which improves the network ability to distinguish between the samples with similar characteristics. The proposed methodology can be used to quickly and quantitatively evaluate the transient stability margin of a power system, and the simulation results validate the effectiveness of the method.**

***Index Terms*—Security region, computer-vision-based power flow image (CVPFI), transient stability margin, convolutional neural network (CNN), comprehensive network.**

I. Introduction

TRANSIENT stability is of great significance to the safe operation of the power grid. The development of fast and accurate methodologies for online transient stability assessment (TSA) is one of the major research topics in power system operation and control.

There are several traditional analysis methods for TSA such as time-domain simulation [1], transient energy function method [2] and extended equal-area criterion [3]. However, the flaws of these methods such as their poor model adaptability and complexity of computation are salient. With the development of wide-area measurement systems (WAMSs), data-driven artificial intelligence (AI) methods provide new opportunities for TSA such as artificial neural network (ANN) [4], support vector machine (SVM) [5] and decision tree (DT) [6]. Recently, deep learning has been widely utilized for online decision-making such as deep belief network (DBN) [7], convolutional neural network (CNN) [8] and long-short-term memory (LSTM) network [9]. Compared with the shallow learning models, the deep learning models have more powerful self-learning ability and higher computational efficiency.

In general, there are two types of application scenarios for these data-driven AI approaches. One scenario is TSA based on stability region, which depends on the post-disturbance dynamic features such as the magnitude of the recovery voltage [10], rotor angles [11], [12] and kinetic energy [13]. The other is TSA based on security region, which chooses steady-state characteristics as the input such as the line flow, load, and generator power [14], [15]. This assessment considers anticipated contingencies. Therefore, preventive control measures can be conducted to withstand potential severe disturbances. However, the aforementioned methods mainly perform qualitative analyses of transient stability problems. In practical applications, the quantitative evaluation of the transient stability margin is most conducive to security prevention and control. Therefore, we focus on the transient stability margin assessment based on security region.

For the input features of the AI model, most previous studies focus on the feature selection and data preprocessing to enhance prediction accuracy. Reference [16] proposes the principle of feature selection, which considers system scale and transient stability mechanism. Reference [17] proposes the dimension reduction approach for the original features, which can shorten the evaluation time. However, a power system is topologically connected by electrical equipment, and the topology information should be considered as the important input feature, which was not discussed in the previous studies.

The AI learning algorithms are improved to predict the transient stability margin more accurately. A DT algorithm is proposed in [12], which improves the prediction accuracy by adding the layers of the network. Reference [18] proposes the TSA model based on CNN, which integrates CNNs with different structures for prediction. However, it is not enough to enhance prediction accuracy only by modifying the structures and parameters of the AI model. Since the characteris-

Manuscript received: July 7, 2020; accepted: October 28, 2020. Date of Cross-Check: October 28, 2020. Date of online publication: November 26, 2020.

This work was supported in part by the National Natural Science Foundation of China (No. 51877034).

J. An (corresponding author), J. Yu, Y. Zhou, and G. Mu are with the Key Laboratory of Modern Power System Simulation and Control & Renewable Energy Technology (Northeast Electric Power University), Ministry of Education, Jilin 132012, China (e-mail: anhuianjun@163. com; yujiachen612@163. com; zhouyiboaa@126.com; mg@neepu.edu.cn).

Z. Li is with China Electric Power Research Institute, Beijing 100192, China (e-mail: lzh624218372@163.com).

DOI: 10.35833/MPCE.2020.000457

tics of the samples near the stability boundary are unclear, it is more likely to be misjudged and will cause poor prediction accuracy. Thus, it is necessary to improve the discrimination ability of the model, especially the samples near the stability boundary to produce higher accurate prediction of the stability margin.

Therefore, a CNN-based comprehensive network is established in this paper to map the relationship between the steady-state information and the transient stability margin of the system under the anticipated contingencies. The proposed network consists of two components. The first classification subnet classifies the samples into the credibly stable/unstable and uncertain categories, and a computer-vision-based power flow image (CVPFI) based on a geographic information system (GIS) is utilized as the input to extract the power flow and topology information of the system. The second prediction subnet further predicts the stability margin of each subclass of the samples through stable prediction subnet, unstable prediction subnet and checking and correction subnet, respectively. A generator stability index [19] is utilized to quantitatively evaluate the stability margin of the system.

The main contributions of this paper are as follows:

1) As the input feature, the proposed CVPFI contains the operation conditions and topology information of the power system. Therefore, the topological variations can be considered in transient stability prediction.

2) By classifying the input samples into different categories, the index prediction subnet of each type is more targeted to the samples of the current class, which can enhance the prediction accuracy. Additionally, it can avoid misjudgment near the stable boundary to the most extent through further checking and correcting of uncertain samples.

The remainder of this paper is organized as follows. Section II illustrates the transformation rule of CVPFI. Section III illustrates the details of the proposed comprehensive neural network for TSA. The interpretability of the prediction results is analyzed in Section IV. Section V presents case study details and discusses the results. Conclusions are made in Section VI.

II. Transformation Rule Based on Steady-state Characteristics

A. Computer-vision-based Power Flow Image

GIS combines the operation information of a power system with geographic location information, which can visually show the operational status of the system based on the electronic map.

Firstly, the administrative division of the regions and the geographical coordinates of the substations and transmission lines are required for the GIS database. Then, a topology connection diagram of the system is established by the visual modeling tool and can be updated in real time.

It is well known that each pixel of an image consists of red, green and blue channels, which can be described by different color values. Therefore, a transformation rule between the steady-state characteristics and the GIS-generated topology diagram can be formulated in this paper to realize the visualization of power flow. The steady-state information is collected by the monitoring system as shown in Table I.

TABLE I
Steady Power Flow of Each Component

Equipment type	Electrical quantity
Generator	Active power output P_G; reactive power output Q_G
Load	Active load P_L; reactive load Q_L
Line	Active power flow P_T; reactive power flow Q_T
Bus	Voltage magnitude U_m; voltage phase angle θ

Assuming that the color value (0-255) of the node in the topology diagram is C_N and that of the transmission line is C_L, the power transmission direction of each line is defined.

The transformation rules of the active or reactive power are as follows:

1) The red channel represents the power levels of the i^{th} node injection and the j^{th} line transmission: $C_{Ni} = P_{Gi} - P_{Li}(Q_{Gi} - Q_{Li})$; $C_{Lj} = P_{Tj}(Q_{Tj})$.

2) The green channel represents the direction of the i^{th} nodal power: when $P_{Gi} - P_{Li}(Q_{Gi} - Q_{Li}) > 0$ (the power is injected into the node), C_{Ni} is set to be the minimum value, and C_{Ni} is set to be the maximum value when $P_{Gi} - P_{Li}(Q_{Gi} - Q_{Li}) < 0$ (the power flows out of the node).

3) The blue channel represents the transmission direction of the j^{th} line power. C_{Lj} is set to be the minimum value when it is consistent with the reference direction. Otherwise, C_{Lj} is set to be the maximum value.

The transformation rules of the voltage are as follows:

1) The red channel represents the voltage magnitude of the i^{th} node: $C_{Ni} = U_{mi}$.

2) The green channel represents the voltage phase angle difference $\Delta\theta$ between the two ends of the j^{th} line: $C_{Lj} = \Delta\theta_j$. Since θ and P have a strong correlation in a high-voltage power system, $\Delta\theta$ can approximately reflect the distribution of the active power in the line.

3) The blue channel represents the direction of $\Delta\theta$ which can reflect the transmission direction of the active power of the j^{th} line. C_{Lj} is set to be the minimum value when it is consistent with the reference direction $\Delta\theta_j > 0$. Otherwise, C_{Lj} is set to be the maximum value.

Since the range of each electrical quantity is different, its value is adaptively matched with the range of pixel color values (0-255) according to (1).

$$C' = \frac{255}{C_{\max} - C_{\min}}(|C| - C_{\min}) \tag{1}$$

where C and C' are the color values before and after matching, respectively; and $C_{\min}$ and $C_{\max}$ are the minimum and maximum absolute value of the electrical quantity, respectively.

After matching, the P-CVPFI (active power), Q-CVPFI (reactive power) and U-CVPFI (voltage) can be generated, and these images are set to be a uniform size according to the topology size. With the transformation rule, the system topology as well as the magnitude and direction of the elec-

trical quantity used is completely retained in CVPFI, enabling the neural network to learn the overall operation state of the system.

Furthermore, the proposed rule exhibits excellent adaptability. Since CVPFIs are transformed based on the online data, when the operation condition changes, the color of the CVPFI varies correspondently. Moreover, based on GIS, a new connection diagram can be generated when the topological structure changes.

B. Quantitative Indices for Evaluating Stability Margin of Power System Under Anticipated Contingencies

To quantitatively evaluate the transient stability margin of the post-disturbance system, the trajectory analysis approach [19] is used to construct the generator stability and instability indices. In the method, the trajectories of the accelerating power and angular velocity of the generator are utilized to analyze the variations in the transient energy of the generators.

The potential energy V_{PEi} trajectories of the i^{th} generator under stable and unstable conditions are shown in Fig. 1.

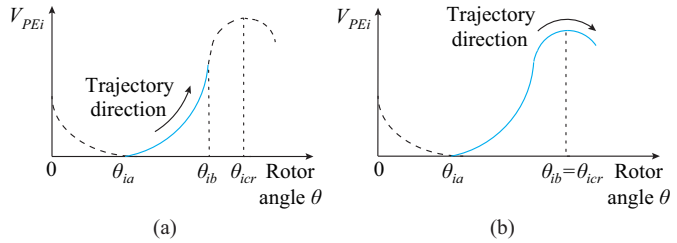

Fig. 1. Trajectories of V_{PEi} under stable and unstable conditions. (a) Stable. (b) Unstable.

In Fig. 1, θ_{ia} and θ_{ib} are the rotor angles when V_{PEi} reaches its first minimum and maximum values, respectively; and θ_{icr} is the critical value of θ_i. If the i^{th} generator is stable, $\mathrm{d}V_{PEi}/\mathrm{d}V_{PEi}\big|_{\theta_{ib}} \neq 0$, and $\mathrm{d}V_{PEi}/\mathrm{d}\theta_i\big|_{\theta_{ib}} = 0$ when it loses the stability. The value of $\mathrm{d}V_{PEi}/\mathrm{d}\theta_i\big|_{\theta_{ib}}$ decreases as θ_{ib} approaches θ_{icr} and finally becomes 0 when $\theta_{ib} = \theta_{icr}$.

Another characteristic of the trajectories is that angular velocity $\omega_i(t_{bi}) = 0$ when the i^{th} generator is stable; otherwise, $\omega_i(t_{bi}) \neq 0$. Obviously, the value of $\omega_i(t_{bi})$ increases as the degree of instability increases.

Therefore, when V_{PEi} reaches its first maximum value, the corresponding stability index S_i and instability index U_i of the i^{th} generator can be defined as in (2) and (3), respectively.

$$S_i = \frac{\left.\dfrac{\mathrm{d}V_{PEi}}{\mathrm{d}\theta_i}\right|_{t_{bi}}}{V_{PEi}(t_{bi}, t_{ai})} = \frac{-P_{ai}(t_{bi})}{V_{PEi}(t_{bi}, t_{ai})} \tag{2}$$

$$U_i = \frac{\omega_N}{2} M_i \frac{|\omega_i(t_{bi})|\omega_i(t_{bi})}{V_{KEi}(t_{ai})} \tag{3}$$

where M_i, P_{ai}, and V_{KEi} are the inertia time constant, accelerating power, and kinetic energy of the i^{th} generator, respectively; and ω_N is the nominal angular velocity.

S_i tends to be zero only when the i^{th} generator is unstable, and U_i is nonzero only when the i^{th} generator loses its stability. This stability index does not depend on any critical energy, and the index value decreases monotonically with the deterioration of stability, which is mathematically proven in [20].

Anticipated contingencies are considered in TSA based on security region. Typically, the system stability margin and the weakest generators with the most severe disturbances are the major focuses for the dispatchers. Thus, the stability and instability indices of the generator with the most severe fault are further selected from the anticipated contingencies, and the concept of the most severe fault is illustrated in Table II.

TABLE II
THE MOST SEVERE FAULT IN ANTICIPATED CONTINGENCY SET

Operation mode	Fault	Index	Generator 1	⋯	Generator i
Unstable mode	Fault M_1	S_1	Zero	⋯	Zero
		U_1	Nonzero	⋯	Nonzero
	⋮	⋮	⋮		⋮
	Fault M_i	S_i	Zero	⋯	Zero
		U_i	Nonzero	⋯	$\max(U_i)$
Stable mode	Fault N_1	S_1	Nonzero	⋯	Nonzero
		U_1	Zero	⋯	Zero
	⋮	⋮	⋮		⋮
	Fault N_j	S_i	Nonzero	⋯	$\min(S_i)$
		U_i	Zero	⋯	Zero

With a given operation mode, if at least one stability index of the generator equals zero and its instability index is nonzero, this operation mode is classified as an unstable operation mode, and the fault with the maximum instability index values is defined as the most severe fault such as fault M_i. In the same operation mode, if stability indices of all generators are nonzero and their instability indices are all zero, this operation mode is classified as a stable operation mode, and the fault with the minimum stability index value is defined as the most severe fault such as fault N_j.

III. TSA BASED ON CNN

CNNs are some of the most commonly used neural networks, which have a strong image processing ability. Since strong recognition ability of CNN for highly nonlinear patterns, it is effective for a number of problems in the fields of both classification and regression.

Therefore, a CNN-based comprehensive network is proposed to predict the generator stability indices under the anticipated contingencies. It consists of a classification subnet and a prediction subnet, and the details of these two subnets are illustrated below.

A. Classification Subnet

To enhance the prediction accuracy of the stability index, the input samples are pre-classified into different categories. Each subclass of samples belongs to the same category with similar characteristics, which enables the subsequent prediction subnet of each type more targeted to the samples of the

current class than the samples of other classes. Therefore, an ensemble CNN-based classification subnet is proposed as shown in Fig. 2.

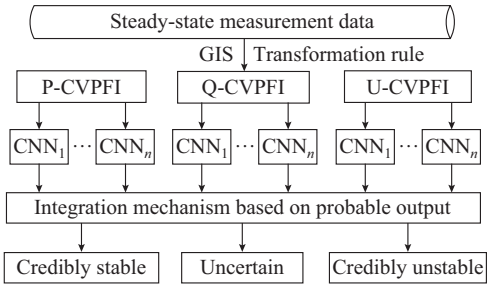

Fig. 2. Ensemble CNN-based classification subnet.

n subclass CNNs are trained by each kind of CVPFI independently, and the optimal structural parameters are determined by the particle swarm optimization (PSO) algorithm. The obtained CNNs are different even with the same network structure because the initial weights and bias are randomly selected.

In practical applications, the training samples are always unbalanced with fewer unstable samples than stable samples, making the model insufficient for learning the features of unstable samples. To avoid this problem, a weighted cross-entropy loss function L_{CE} is adopted in the classification model as shown in (4).

$$L_{CE}=-\frac{1}{N}\left[\mu y_i \lg \bar{y}_i+(1-y_i)\lg(1-\lg \bar{y}_i)\right] \tag{4}$$

where N is the total number of training samples; and y_i and $\bar{y}_i$ are the actual and predicted labels of the i^{th} sample, respectively; and μ is the cost weight of the positive samples (unstable samples), which is set as the ratio of the number of stable samples to the number of unstable samples.

The output of each kind of classifier is the average of probabilistic outputs for the corresponding subclass CNN:

$$P(C_k|X)=\frac{\sum_{i=1}^{n} p_i(C_k|X)}{n} \quad k=0,1 \tag{5}$$

where $p_i(C_k|X)$ is the probability of category C_k with respect to sample X in the i^{th} CNN. The evaluation result $y_{pred}(X)$ of each kind of classifier is:

$$y_{pred}(X)=\begin{cases}0 & P(C_0|X)\geq\gamma(P(C_1|X)<1-\gamma)\\ 1 & P(C_0|X)<\gamma(P(C_1|X)\geq 1-\gamma)\end{cases} \tag{6}$$

where $P(C_0|X)$ and $P(C_1|X)$ are the probabilities that X is identified as stable and unstable, respectively; and γ is the discriminative threshold, which is normally set to be 0.5.

The integrated decision-making rules are defined as follows: X will be classified as stable only when all the evaluation results are 0, and X will be classified as unstable only when all the evaluation results are 1. Otherwise, the sample is regarded as uncertain and needs to be further distinguished. Therefore, the proposed classification subnet can identify the credibly stable/unstable samples and uncertain samples.

B. Prediction Subnet

The categorized samples received from the classification subnet are further processed in the prediction subnet to predict the generator stability indices under the anticipated contingencies, which is shown in Fig. 3.

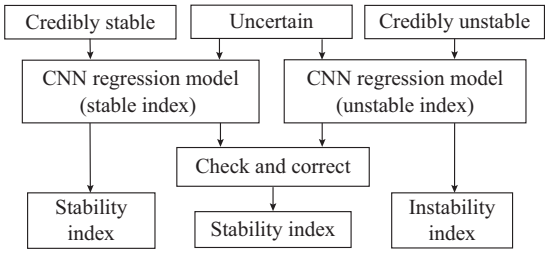

Fig. 3. Prediction subnet.

With U-CVPFI as the input, the stable and unstable prediction subnets are trained by the corresponding samples, and the L_2 loss function shown in (7) is generally adopted in the regression model.

$$L_2=\frac{1}{2N}\sum_{i=1}^{N}(\bar{y}_i-y_i)^2 \tag{7}$$

After training with adequate number of samples, credibly stable/unstable samples are sent to the corresponding prediction subnet, where the stability/instability indices are predicted.

Uncertain samples always contain both stable and unstable characteristics, so it is more likely to be misjudged. To further improve the ability of the model to distinguish between similar characteristics, these samples are sent to both the stable and unstable prediction subnets. Considering the conservatism of power grid operation, the uncertain sample will be judged as stable only when all instability indices equal zero. If at least one of the instability indices is nonzero, this sample will be defined unstable. Based on the cross checking and cross-correction, these uncertain samples can be precisely classified into stable/unstable subsets, and their stability/instability indices can be further predicted by the corresponding regression model.

The aforementioned method actually takes the intersection of two prediction subnets to assess generator stability margin. Therefore, the misjudgment of the model near the stability boundary is avoided as far as possible, and the accuracy of TSA can be improved.

C. Assessment Process

The block diagram of TSA is shown in Fig. 4. It includes two components: offline training and online application. The detailed procedures are as follows:

1) Offline Training

Step 1: collect the historical data from different power system conditions to generate the corresponding CVPFIs which are used as the input of the model.

Step 2: calculate the stability and instability indices under the anticipated contingencies for each sample, and further select the indices with the most severe faults as the output.

Step 3: construct the CNN-based comprehensive network and train the model by using the back-propagation algorithm

to fine-tune all parameters in a supervised way.

2) Online Application

Step 4: obtain online steady-state data and convert it to CVPFIs through GIS and the transformation rule.

Step 5: input CVPFIs into the trained model and predict the generator stability indices online, which will provide the dispatchers with operation reference.

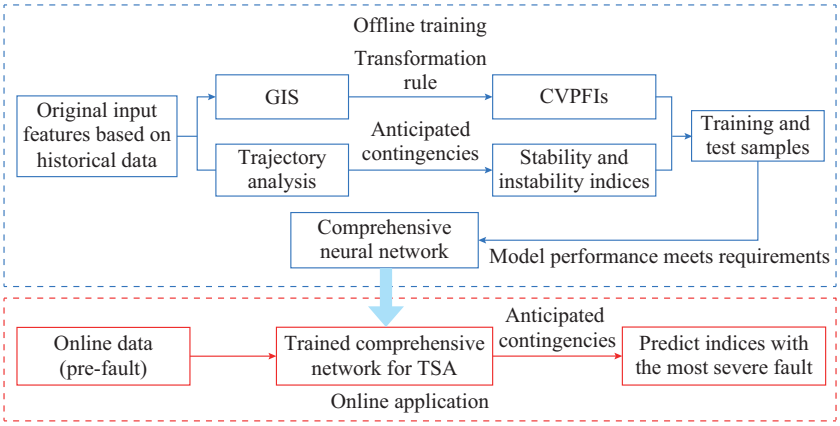

Fig. 4 Framework of TSA.

It should be pointed out that several different topologies of the power grid can be utilized to train the proposed model and improve its adaptability to topological variations. Through the above prediction method, the transient stability margin under the anticipated contingencies can be accurately predicted through the steady-state information online.

D. Model Performance

A useful tool to evaluate the ability of a neural network and perform TSA is the confusion matrix, which is shown in Table III, where *TP* and *TN* are the stable and unstable samples that are correctly identified, respectively; *FN* are false negative samples, i. e., the stable samples that are falsely identified as unstable; *FP* are false positive samples, i.e., the unstable samples that are falsely identified as stable.

TABLE III
CONFUSION MATRIX

Confusion matrix	Stable (predicted)	Unstable (predicted)
Stable (actual)	*TP*	*FN*
Unstable (actual)	*FP*	*TN*

The accuracy rate *AC* indicates the proportion of correctly classified samples as shown in (8).

$$AC = \frac{TP + TN}{TP + FN + FP + TN} \tag{8}$$

The false alarm rate *FA* indicates the proportion of false negative samples, i. e., the stable samples that are falsely identified as unstable, as shown in (9).

$$FA = \frac{FN}{TP + FN} \tag{9}$$

The false dismissal rate *FD* indicates the proportion of false positive samples, i. e., the unstable samples that are falsely identified as stable, as shown in (10).

$$FD = \frac{FP}{FP + TN} \tag{10}$$

In addition, the average error E_{rr} is used to evaluate the prediction accuracy of the neural network, as shown in (11).

$$E_{rr} = \frac{1}{N}\sum_{i=1}^{N}\left| s_i - r_i \right| \tag{11}$$

where s_i and r_i are the predicted value and actual value of the stability index in the i^{th} sample, respectively.

IV. Interpretability Analysis of CNN

Although CNN performs well, it remains a black box. It is important to understand the reasons behind predictions, which is the basis of engineering application. In this paper, a linear surrogate model [21] is constructed to explain the predictions of the stable regression model and help the dispatchers verify the credibility of the prediction results.

Although a linear model is difficult to explain globally, in the local neighborhood, the surrogate model $g(z)$ can be used as a reasonable approximation of the original model $f(x)$:

$$g(z) = \omega_0 + \sum_{i=1}^{M}\omega_i z_i \approx f(x) \tag{12}$$

where x is the input of CNN; and z is M important variables that have the greatest impact on stability. By optimizing the objective function of $g(z)$, ω_i is obtained as the interpretation result. The process is shown in Fig. 5.

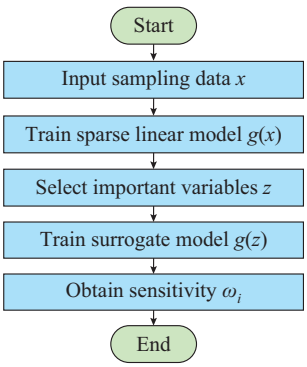

Fig. 5. Construction of surrogate model.

Firstly, the training set $\{x_1', x_2', ..., x_N'\}$ around (x_0, y_0) is sampled for interpretation, and $\{y_1, y_2, ..., y_N\}$ are the corresponding minimum stability indices in CNN. The sampling data follow the multivariate Gaussian distribution $N(x_0, \boldsymbol{\Sigma})$ and $\boldsymbol{\Sigma}$ is the covariance matrix of the training data.

Then, based on the elastic network, a sparse linear model $\tilde{g}(x)$ is constructed to select the important variables, which can highlight the main factors affecting the stability. The objective function can be defined as:

$$\min_{\omega}\left[L(\omega)+\sum_{i=1}^{N}\rho(x_i')(y_i-g(x_i'))^2\right] \tag{13}$$

where $L(\omega)$ is composed of L_1 and L_2 regularization, i. e., $L(\omega)=\lambda\left[\alpha\omega_I^2+(1-\alpha)\left|\omega_i\right|\right]$, and α is used to adjust the proportion of the two norms; $g(x_i')$ is trained repeatedly by adjusting λ; and $\rho(x_i')$ is the weight of the sampling data, which can be calculated by the Gaussian kernel function:

$$\rho(x_i')=\mathrm{e}^{-\frac{1}{2\delta^2}\left\|x_i'-x_0\right\|_2^2} \tag{14}$$

where δ is the free parameter related to the fitting range of the linear model.

Finally, using the important feature set z as the input, the linear ridge regression function is further used as the surrogate model, and its objective function is the same as (13), in which $L(\omega)$ adopts L_2 regularization, i. e., $L(\omega)=\lambda\sum_{i=1}^{M}\omega_i^2$. Hence, the parameter deviation will be reduced. The model parameter ω can be obtained when $g(z)\approx f(x)$, which represents the sensitivity between the state variable and the stability status.

V. Case Studies and Discussions

A. IEEE 39-bus System

1) Construction of Sample Set

The simulations and tests are implemented on a PC with an Intel Core i7-8700 CPU and 16 GB of RAM, and the real-time measurement is replaced by the simulated data. As shown in Fig. 6, the proposed method is tested with IEEE 39-bus system first, which is partitioned into 3 regions according to the directions of the power transfers.

Based on the partition, three-phase faults on 6 transmission lines connecting different regions are used to construct the anticipated contingency set. Each fault is simulated at 50% of the line length and is cleared in 0.2 s. For a certain operation condition, the system load level is varied between 80% and 120% of the base load, and the most severe fault in this operation mode can be further selected.

The steady-state characteristics of each sample are converted into different CVPFIs, and the input and the stability or instability indices of 10 generators in the fault mode are taken as the output. We generate an input space of 10200 samples in various operation modes. A total of 9000 samples are randomly selected from the 10200 samples as training set. The remaining 1200 samples are used as testing set as shown in Table IV.

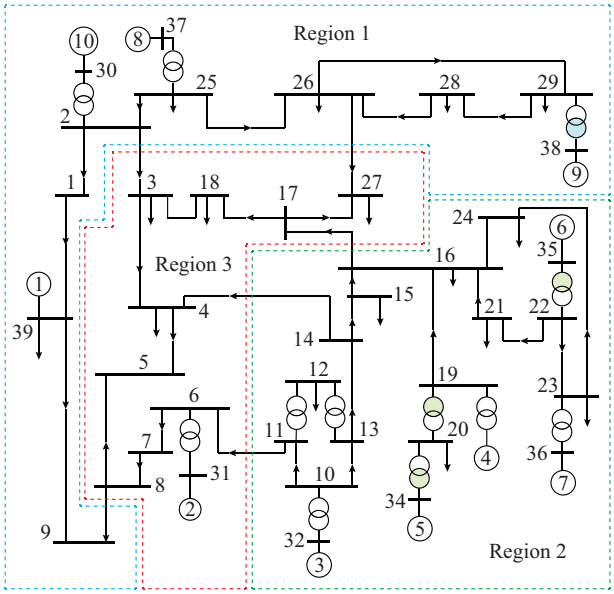

Fig. 6. IEEE 39-bus system.

TABLE IV
Training and Testing Sets of IEEE 39-bus System

Set type	Number of stable sample	Number of unstable sample	Total number of sample
Training	5471	3529	9000
Testing	744	456	1200

2) Model Performance

Each CNN classifier in the classification subnet has two convolutional and max pooling layers, two fully connected hidden layers and a softmax layer at the end. The initial learning rate, iteration numbers and batch sample numbers of CNN are 0.001, 1000 and 100, respectively. The Adam stochastic optimization algorithm with a variable learning rate is adopted to minimize the loss function.

PSO is used to select the optimal convolution kernel number (k_1, k_2) and size (l_1, l_2) of each subclass CNN. The acceleration constants c_1 and c_2 are 0.5 and 1.5, respectively, and the prediction error rate is taken as the fitness function. After optimization, the structural parameters of each subclass CNN are shown in Table V.

TABLE V
Structural Parameters of Subclass CNNs

Subclass CNN	k_1	k_2	l_1	l_2
P-CVPFI	5	10	3	3
Q-CVPFI	6	12	5	5
U-CVPFI	6	12	4	4

The reasonability of the input features has a great influence on the performance of the classifier, and the following two feature sets are used as the inputs.

Feature set 1: the original features are arranged into a 2D matrix sequentially.

Feature set 2: the original features are converted into CVPFIs by the proposed method.

The prediction accuracy of the classification subnet is shown in Fig. 7.

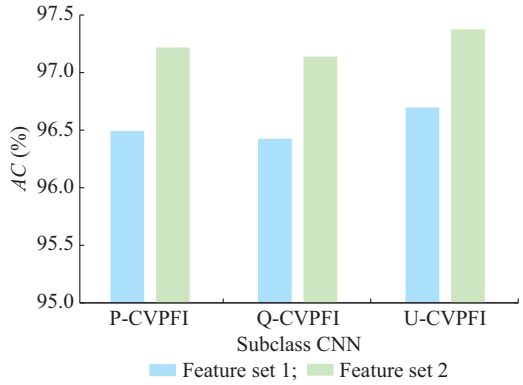

Fig. 7. Prediction accuracy of subclass CNNs.

The comparison results show that the accuracy of the model with feature set 2 is significantly higher than that of the model with feature set 1, indicating that the topology and power flow information contained in CVPFIs can accurately reflect the operation state of the system.

Then, U-CVPFI with the best classification performance is taken as the input, and DT, SVM and MLP classifiers are selected for comparison. DT selects the C5.0 algorithm, the optimal structure parameters of SVM are determined by 5-fold cross-validation, and the kernel sizes of the four fully connected layers in MLP classifier are 100, 50, 10 and 2, respectively. Table VI shows the performance of different classifiers for the testing datasets.

TABLE VI
ASSESSMENT RESULTS OBTAINED BY DIFFERENT CLASSIFIERS

Classifier	*AC* (%)	*FA* (%)	*FD* (%)
DT	95.42	3.76	5.92
SVM	96.08	3.36	4.82
MLP	96.25	3.23	4.61
CNN	97.33	2.28	3.29

Table VI shows that CNN performs the best and has the highest prediction accuracy, indicating that the local connection and weight sharing features of the convolutional layer in the CNN have a strong ability to extract features from images. Moreover, different numbers of classifiers are selected for integration, and the prediction accuracies of each subclass CNNs for the testing datasets are shown in Fig. 8.

As the number of subclass CNNs increases, the prediction performance improves rapidly. Only 4 individual integrated CNN classifiers can achieve high accuracy. This is because the misclassified samples can be corrected after comprehensive judgment by multiple classifiers. However, restricted by the input feature information, the prediction performance is basically similar when more than 6 classifiers are integrated. Considering the calculation speed and prediction performance, n is set as 4 for each kind of CVPFI.

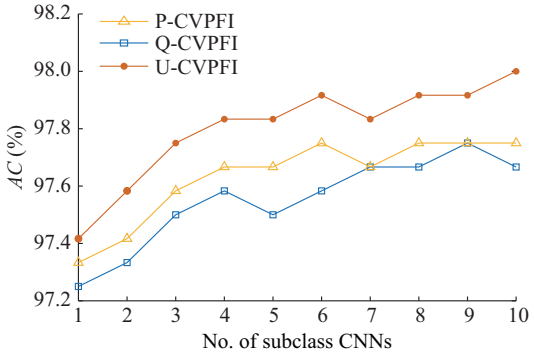

Fig. 8. Prediction accuracy of subclass CNNs.

Besides, three different index prediction methods are considered to further compare the effectiveness of the proposed comprehensive network.

1) Method 1: the stable and unstable indices are predicted directly for the original unclassified samples.

2) Method 2: the original samples are divided into the stable and unstable categories through the classification network, and the corresponding indices are predicted.

3) Method 3: the indices of the samples are predicted by the proposed comprehensive network in this paper.

The parameters of the CNN regression model in the prediction subnet are the same as those of the classification model, and the predicted index error for each generator is shown in Fig. 9.

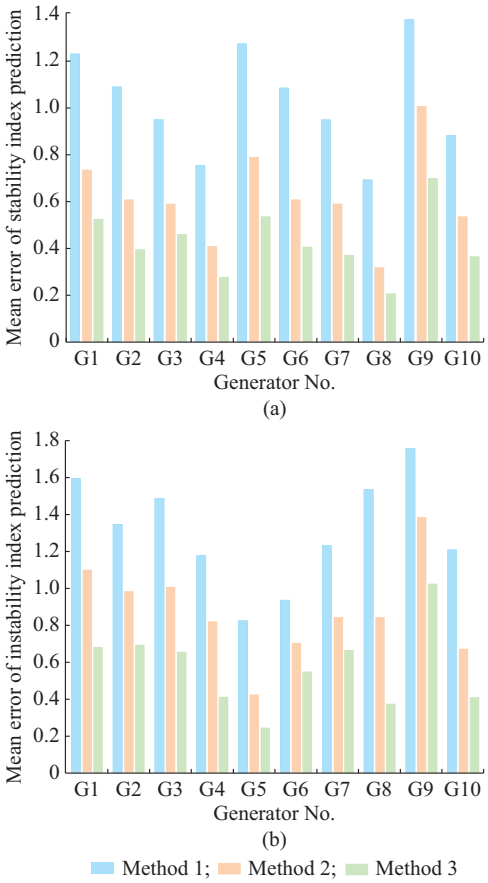

Fig. 9. Mean error of predicted index. (a) Stability index. (b) Instability index.

We can observe that the performances of method 2 and method 3 are significantly better than that of method 1. The main reason is that if the raw training samples are not classified, they may not be sent into the subnet of the corresponding type. In contrast, method 2 and method 3 can make the subnet of each type more targeted to the samples of the current class than method 1, and the learning efficiency of the prediction subnets can be improved. The performances of different methods are shown in Table VII.

TABLE VII
ASSESSMENT RESULTS OBTAINED BY DIFFERENT PREDICTION METHODS

Prediction method	*AC* (%)	*FA* (%)	*FD* (%)	E_{rr}
Method 1	96.92	2.55	3.74	0.9638
Method 2	97.83	1.88	2.63	0.4371
Method 3	98.75	1.21	1.32	0.2246

We can observe that method 3 has the best performance, and its false dismissal rate is substantially lower than that of method 2. The reason lies in the cross-checking and cross-correction of the uncertain samples, which can accurately predict the stability indices of critical samples. As a result, the proposed comprehensive network achieves great prediction performance.

3) Analysis of Model Adaptivity

Since the training and testing samples are randomly selected from a total dataset, the operation conditions in the testing set may exist in the training set. However, in practical applications, the operation modes cannot be the same as those of the offline simulation scenarios. Therefore, it is necessary to verify the adaptivity of the proposed model to different scenarios.

Firstly, the new testing sets are constructed by setting different load levels, simulating the variation in operation situation. The performances of the proposed model for those new testing sets are shown in Table VIII.

TABLE VIII
PREDICTION RESULTS OF TESTING SETS WITH DIFFERENT POWER FLOWS

Testing set	Fluctuation range of base load (%)	*AC* (%)	E_{rr}
Dataset 1	80-120	98.50	0.2246
Dataset 2	100-150	98.16	0.2597
Dataset 3	150-200	97.83	0.3053
Dataset 4	200-300	97.58	0.3374

Table VIII shows that the proposed model performs well when the operation condition changes. Then, the system load level is set as 80%-120% of the base load, and the performances of the model with different network configurations are shown in Table IX. Table IX shows that the model can produce accurate prediction when the topology changes. In particular, when region 1 has been split from the original system (dataset 5), the accuracy of the model is still up to 97.42%, indicating that the proposed model has strong generalizability.

TABLE IX
PREDICTION RESULTS OF TESTING SETS WITH DIFFERENT NETWORK CONFIGURATIONS

Testing set	Network configuration	*AC* (%)	E_{rr}
Dataset 1	All the lines are in service	98.50	0.2246
Dataset 2	Line 2-3 is out of service	98.33	0.2521
Dataset 3	Lines 2-3 and 6-11 are out of service	98.08	0.2904
Dataset 4	Lines 2-3, 6-11 and 4-14 are out of service	97.75	0.3157
Dataset 5	Lines 2-3, 8-9 and 26-27 are out of service	97.42	0.3513

4) Analysis of Model Conservatism

Table X shows the comparison of the performances before and after the improvement of the cross-entropy loss function.

TABLE X
COMPARISON OF CLASSIFICATION PERFORMANCE RESULTS

Cross-entropy loss function	*AC* (%)	*FA* (%)	*FD* (%)
Before improvement	97.75	1.88	2.85
After improvement ($\mu = 1.56$)	98.17	1.75	1.97

After the improvement of the loss function, the classifier performs better and has a lower false dismissal rate, indicating that the correction of the weight coefficient can effectively enhance the ability of the model to fit unstable samples.

To further reduce the number of false positive samples, the discriminative threshold γ of the classification model can be adjusted, and the evaluation indices of the comprehensive network with different values of γ are shown in Fig. 10.

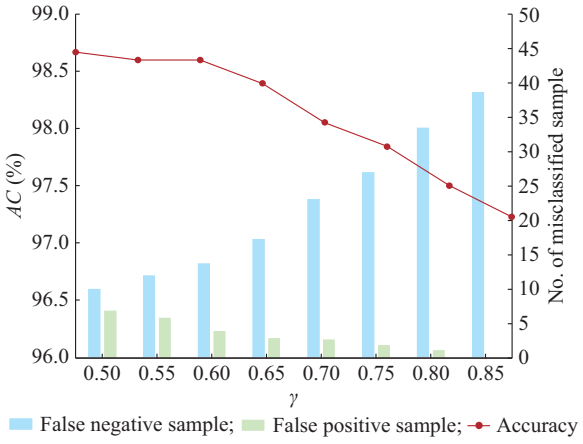

Fig. 10. Assessment results with different discriminative thresholds.

As shown in Fig. 10, as γ increases, the number of false positive samples decreases gradually. There are no false positive samples ($FD = 0$) when γ increases to 0.85, indicating the effectiveness in setting the threshold. A higher value of γ also gives rise to more false negative samples, resulting in a reduction of accuracy. However, the false negative samples have little impact on the stability of the power system. When γ is set to be 0.85, the accuracy only drops to 97.33%, which basically meets the requirement.

In an actual operation, the dispatcher can select a reasonable threshold. By paying attention to the prediction accura-

cy, γ can be set to be a low value. Moreover, γ can be set to be a high value to avoid unstable samples being falsely identified as stable.

5) Analysis of Model Interpretability

The trained CNN regression model is taken as the object to be explained. U_m and θ are selected as the training set of the surrogate model. The kernel parameter of the surrogate model is $\delta=3$. By power grid searching, $\alpha=0.5$ and $\lambda=0.4$ are finally obtained as the general parameters.

Firstly, 50 samples are randomly selected from the testing set to construct the surrogate model, and the relative error between the surrogate model and the original model is shown in Fig. 11, where the horizontal axis is the neighborhood range ϕ of the samples that follow $N(x_0, \phi\boldsymbol{\Sigma})$.

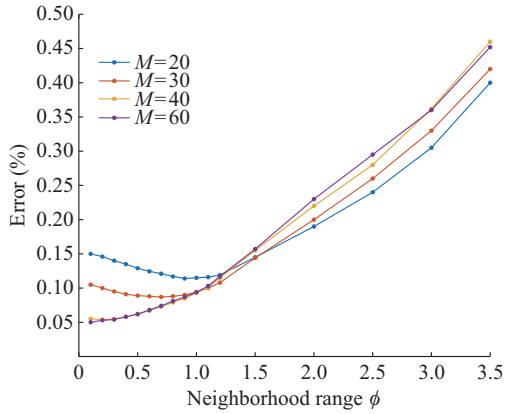

Fig. 11. Error of surrogate models.

When ϕ is less than 1, the surrogate model with the largest M value has the highest fitting accuracy, which decreases when ϕ increases further. On the whole, there is little relative error, which proves the rationality of the proposed surrogate model.

Then, the dataset X_c, whose loads in regions 1, 2 and 3 are 120%, 100% and 80% of the base load levels, respectively, is selected from the testing set. One of the data points is selected from X_c for interpretation ($M=40, \phi=0.5$), and the variables with the greatest absolute sensitivity values are shown in Table XI.

TABLE XI
INTERPRETATION RESULTS OF SURROGATE MODEL

Feature	ω_i	Feature	ω_i
U_{m30}	0.026	$\theta_{3\text{-}25}$	0.016
U_{m18}	–0.024	U_{m9}	0.014
$\theta_{25\text{-}26}$	0.023	U_{m5}	0.013
$\theta_{1\text{-}39}$	0.023	$\theta_{8\text{-}9}$	–0.011
$\theta_{14\text{-}15}$	–0.022	U_{m23}	0.009
U_{m37}	0.020	$\theta_{26\text{-}27}$	–0.008
$\theta_{6\text{-}11}$	–0.019	$\theta_{3\text{-}18}$	–0.007
U_{m39}	0.018	U_{m21}	0.006

The load of region 1 is the largest in X_c and has a great impact on the transient stability of the system. In Table XI, the variables of region 1 have the greatest sensitivities to the transient stability margin. Meanwhile, the power is transmitted from region 3 to region 1, where the transmission channel is relatively important. Table XI shows that the influences of bus voltage and line power (proportional to θ) on channels are relatively large, which is consistent with the reality. Therefore, the interpretable model reveals the influence of the state variable on the stability, which enhances the accuracy of the prediction results.

B. IEEE 118-bus System

IEEE 118-bus system is used to further verify the applicability of the proposed method in a complex power grid. The created anticipated contingency sets are three-phase faults on the main transmission lines, and the fault clearing time is varied from 0.14 s to 0.18 s to obtain a total of 13460 contingencies. The ratio of the training samples to the testing samples is approximately equal to that of IEEE 39-bus system, as shown in Table XII.

TABLE XII
TRAINING AND TESTING SETS OF 118-BUS SYSTEM

Set type	Number of stable sample	Number of unstable sample	Total number of sample
Training	7176	4684	11960
Testing	973	527	1500

The construction method of the samples is the same as that of IEEE 39-bus system, which includes three kinds of CVPFIs and the stability or instability indices of 54 generators with the most severe faults. The parameters of the proposed model are optimized by PSO, and the performance of the model in different systems is shown in Table XIII.

TABLE XIII
ASSESSMENT OF PREDICTION RESULTS

System	*AC* (%)	*FA* (%)	*FD* (%)	E_{rr}
IEEE 39-bus	98.75	1.21	1.32	0.2246
IEEE 118-bus	98.67	1.34	1.52	0.2313

We can observe that the model in IEEE 118-bus system still achieves high prediction performance, which verifies that the proposed method can be applied to more complex power grids. Moreover, the conservatism of the model can be further improved by adjusting the discriminative threshold γ. According to the test, there are no false positive samples ($FD=0$) when γ increases to 0.83. The accuracy is still 97.5%, which meets the operation requirements.

In addition, the testing time of IEEE 39-bus and IEEE 118-bus systems are 226.52 s and 372.08 s, respectively, which is slightly long but still acceptable because the training process is conducted offline. Considering the time delay of data transmission (taking 50 ms as an example), the testing time of IEEE 39-bus and IEEE 118-bus systems for one sample are 0.054 s and 0.055 s, respectively, which can meet the requirements of online TSA. In practical applications, the computation time can be reduced by using an optimized code in a lower-level programming language.

VI. Conclusion

A novel methodology for online stability margin assessment is proposed in this paper. Based on a GIS, a computer-vision-based power flow image is proposed as the input to extract the power flow and topology information of the system. A comprehensive neural network is established to predict the generator stability indices under the anticipated contingencies. Through the pre-classification of the input samples and checking and correcting of the uncertain samples, the prediction accuracy of the proposed model is improved and the misjudgment near the stable boundary is avoided as far as possible.

The major advantage of the proposed methodology is that only steady-state information is used in the online stability margin prediction process, which can avoid the time consumption of simulated calculations and provide the power grid dispatchers with operation reference.

In future research, we will further investigate the essential factors that affect generator stability indices, aiming to establish practical and detailed strategies for preventive control. Deep reinforcement learning is a potential measure to carry out the studies on preventive control.

References

[1] S. Zadkhast, J. Jatskevich, and E. Vaahedi, "A multi-decomposition approach for accelerated time-domain simulation of transient stability problems," *IEEE Transactions on Power Systems*, vol. 30, no. 5, pp. 2301-2311, Oct. 2014.

[2] P. Bhui and N. Senroy, "Real-time prediction and control of transient stability using transient energy function," *IEEE Transactions on Power Systems*, vol. 32, no. 2, pp. 923-934, May 2016.

[3] Y. Xue, T. Van Cutsem, and M. Ribbens-Pavella, "A simple direct method for fast transient stability assessment of large power systems," *IEEE Transactions on Power Systems*, vol. 3, no. 2, pp. 400-412, May 1988.

[4] S. Tso, X. Gu, Q. Zeng *et al*., "An ANN-based multilevel classification approach using decomposed input space for transient stability assessment," *Electric Power Systems Research*, vol. 46, no. 3, pp. 259-266, Apr. 1998.

[5] F. R. Gomez, A. D. Rajapakse, U. D. Annakkage *et al*., "Support vector machine-based algorithm for post-fault transient stability status prediction using synchronized measurements," *IEEE Transactions on Power Systems*, vol. 26, no. 3, pp. 1474-1483, Aug. 2011.

[6] K. Sun, S. Likhate, V. Vittal *et al*., "An online dynamic security assessment scheme using phasor measurements and decision trees," *IEEE Transactions on Power Systems*, vol. 22, no. 4, pp. 1935-1943, Nov. 2007.

[7] Q. Zhu, J. Dang, J. F. Chen *et al*., "A method for power system transient stability assessment based on deep belief networks," *Proceedings of the CSEE*, vol. 38, no. 3, pp. 735-743, Mar. 2018.

[8] B. Tan, J. Yang, X. Pan *et al*., "Representational learning approach for power system transient stability assessment based on convolutional neural network," *Institution of Engineering and Technology*, vol. 2017, no. 13, pp. 1847-1850, Nov. 2017.

[9] J. Q. James, A. Y. Lam, D. J. Hill *et al*., "Intelligent time-adaptive transient stability assessment system," *IEEE Transactions on Power Systems*, vol. 33, no. 1, pp. 1049-1058, May 2017.

[10] F. R. Gomez, A. D. Rajapakse, U. D. Annakkage *et al*., "Support vector machine-based algorithm for post-fault transient stability status prediction using synchronized measurements," *IEEE Transactions on Power Systems*, vol. 26, no. 3, pp. 1474-1483, Aug. 2011.

[11] J. Geeganage, U. D. Annakkage, T. Weekes *et al*., "Application of energy-based power system features for dynamic security assessment," *IEEE Transactions on Power Systems*, vol. 30, no. 4, pp. 1957-1965, Jul. 2015.

[12] M. He, J. Zhang, and V. Vittal, "Robust online dynamic security assessment using adaptive ensemble decision-tree learning," *IEEE Transactions on Power Systems*, vol. 28, no. 4, pp. 4089-4098, Nov. 2013.

[13] N. Amjady and S. F. Majedi, "Transient stability prediction by a hybrid intelligent system," *IEEE Transactions on Power Systems*, vol. 22, no. 3, pp. 1275-1283, Aug. 2007.

[14] M. He, V. Vittal, and J. Zhang, "Online dynamic security assessment with missing PMU measurements: a data mining approach," *IEEE Transactions on Power Systems*, vol. 28, no. 2, pp. 1969-1977, May 2013.

[15] Y. Xu, Z. Dong, J. Zhao *et al*., "A reliable intelligent system for real-time dynamic security assessment of power systems," *IEEE Transactions on Power Systems*, vol. 28, no. 3, pp. 1235-1263, Aug. 2012.

[16] L. Guan and S. Tao, "Combination of heuristic reasoning and ANN to realize on-line transient stability assessment in large scale power systems," *Automation of Electric Power Systems*, vol. 24, no. 2, pp. 22-26, Feb. 2000.

[17] J. Geeganage, U. Annakkage, T. Weekes *et al*., "Application of energy-based power system features for dynamic security assessment," *IEEE Transactions on Power Systems*, vol. 30, no. 4, pp. 1957-1965, May 2015.

[18] Y. Zhou, Q. Guo, H. Sun *et al*., "A novel data-driven approach for transient stability prediction of power systems considering the operational variability," *International Journal of Electrical Power & Energy Systems*, vol. 11, no. 107, pp. 379-394, May 2019.

[19] G. Mu, Z. Wang, Y. Han *et al*., "A new method for quantitative assessment of the transient stability of power systems-Trajectory analysis method," *Proceedings of the CSEE*, vol. 13, no. 3, pp. 23-30, May 1993.

[20] G. Mu, Z. Wang, Y. Han *et al*., "A proof on property of the stability measurement function $S_i(t)$ and validity of the stability index S_i," *Proceedings of the CSEE*, vol. 4, no. 2, pp. 60-65, Mar. 1994.

[21] M. T. Ribeiro, S. Singh, and C. Guestrin, "Why should I trust you? Explaining the predictions of any classifier," in *Proceedings of the 22nd ACM SIGKDD International Conference on Knowledge Discovery and Data Mining*, San Francisco, USA, Aug. 2016, pp. 1135-1144.

Jun An received the B.S and M.S. degrees in electrical engineering from Northeast Electric Power University, Jilin, China, in 1999 and 2002, respectively, and Ph.D. degree in electrical engineering from North China Electric Power University, Baoding, China, in 2010. He is a Professor at the School of electrical engineering at Northeast Electric Power University. His research interests include power system stability and control.

Jiachen Yu received the B.S. degree in energy and power engineering from Northeast Electric Power University, Jilin, China, in 2014. He is currently pursuing the M.S. degree at Northeast Electric Power University. His research interests include power system stability and control.

Zonghan Li received the B.S. and M.S. degrees in electrical engineering from Northeast Electric Power University, Jilin, China, in 2011 and 2015, respectively. He is currently pursuing the Ph.D. degree in China Electric Power research institute, Beijing, China. His research interests include power system stability and control.

Yibo Zhou received the B.S. degree in electrical engineering from North China Electric Power University, Beijing, China, in 2011 and the M.S. degree in electrical engineering from Northeast Electric Power University, Jilin, China, in 2015. He is currently pursuing the Ph. D. degree in Northeast Electric Power University. His research interest includes power system optimization.

Gang Mu received the Ph. D. degree in electrical engineering from Tsinghua University, Beijing, China, in 1991. He is currently a Professor with Northeast Electric Power University, Jilin, China. He is a Fellow and a Councilor of Chinese Society for Electrical Engineering (CSEE). He is also the Director of the Modern Power System Simulation and Control and Renewable Energy Technology Key Laboratory of Ministry of Education, Jilin, China. His research interests include power system stability analysis, planning and operation analysis of large-scale wind farms integrating to power systems, planning and control of energy storage, and big data and AI applications in power system operation.